AGU PUBLICATIONS

JGR

Journal of Geophysical Research: Space Physics

RESEARCH ARTICLE
10.1002/2016JA022638

Special Section:
Measurement Techniques in Solar and Space Physics: Optical and Ground-Based

Monte Carlo simulation of the neutron monitor yield function

P.-S. Mangeard[1,2,3], D. Ruffolo[2], A. Sáiz[2], S. Madlee[2], and T. Nutaro[4]

[1]National Astronomical Research Institute of Thailand, Chiang Mai, Thailand, [2]Department of Physics, Faculty of Science, Mahidol University, Bangkok, Thailand, [3]Now at Department of Physics and Astronomy, University of Delaware, Newark, Delaware, USA, [4]Department of Physics, Faculty of Science, Ubon Ratchathani University, Ubon Ratchathani, Thailand

Abstract Neutron monitors (NMs) are ground-based detectors that measure variations of the Galactic cosmic ray flux at GV range rigidities. Differences in configuration, electronics, surroundings, and location induce systematic effects on the calculation of the yield functions of NMs worldwide. Different estimates of NM yield functions can differ by a factor of 2 or more. In this work, we present new Monte Carlo simulations to calculate NM yield functions and perform an absolute (not relative) comparison with the count rate of the Princess Sirindhorn Neutron Monitor (PSNM) at Doi Inthanon, Thailand, both for the entire monitor and for individual counter tubes. We model the atmosphere using profiles from the Global Data Assimilation System database and the Naval Research Laboratory Mass Spectrometer, Incoherent Scatter Radar Extended model. Using FLUKA software and the detailed geometry of PSNM, we calculated the PSNM yield functions for protons and alpha particles. An agreement better than 9% was achieved between the PSNM observations and the simulated count rate during the solar minimum of December 2009. The systematic effect from the electronic dead time was studied as a function of primary cosmic ray rigidity at the top of the atmosphere up to 1 TV. We show that the effect is not negligible and can reach 35% at high rigidity for a dead time >1 ms. We analyzed the response function of each counter tube at PSNM using its actual dead time, and we provide normalization coefficients between count rates for various tube configurations in the standard NM64 design that are valid to within ~1% for such stations worldwide.

Key Points:
- We calculated the neutron monitor (NM) yield function by Monte Carlo simulation of cosmic ray-induced interactions in the atmosphere and NM
- The simulated count rate due to cosmic rays for an NM at Doi Inthanon, Thailand, matches observations to within 9%
- We calculated effects of the geomagnetic field and dead time and normalization coefficients for common NM64 detector configurations

Correspondence to:
D. Ruffolo,
david.ruf@mahidol.ac.th

Citation:
Mangeard, P.-S., D. Ruffolo, A. Sáiz, S. Madlee, and T. Nutaro (2016), Monte Carlo simulation of the neutron monitor yield function, *J. Geophys. Res. Space Physics*, *121*, 7435–7448, doi:10.1002/2016JA022638.

Received 29 FEB 2016
Accepted 9 AUG 2016
Accepted article online 11 AUG 2016
Published online 27 AUG 2016

1. Introduction

Neutron monitors (NMs) detect atmospheric secondary particles (SPs)—mostly neutrons—that reach the ground. Those SPs are produced by the interaction of primary cosmic ray particles in the Earth's atmosphere. The dominant contribution to the NM count rate comes from Galactic cosmic rays (GCRs) at GV range rigidity. The GCR flux reaching the top of Earth's atmosphere is modulated by the solar wind and heliospheric magnetic field, and thus, time variations in the NM count rate indicate time variations in solar activity. NMs in the worldwide network are the premier instruments to track the time variations of the GCR flux that are induced by the solar activity, and each NM has its own cutoff (threshold) rigidity, P_c, due to Earth's atmosphere and geomagnetic field depending on the NM location. In the case of short-term variations, such as ground level enhancements (GLEs) following some major solar flares and/or coronal mass ejections, the time profile of the event can be studied with a precision of a minute or better [*Bieber et al.*, 2013]. Note that during a GLE, the count rate can be dominated by solar energetic particles. The long-term variations in GCRs (11 and 22 year cycles) can be observed with a relative uncertainty of <1%.

In order to correctly interpret the count rate of a single NM, it is crucial to determine its yield function, i.e., the response of the detector (number of counts recorded) per unit intensity of primary particles (PP). This is usually expressed as a function of the rigidity and the type of PP at the top of the atmosphere. The yield function depends on the location of the detector (latitude, longitude, and altitude), the density profile of the atmosphere over the detector, the considered incidence angle of the PP, the geomagnetic field, and the intrinsic characteristics of the NM and its surrounding structure. Recently, with the increase of computational capabilities, large efforts were undertaken to parametrize this function using Monte Carlo (MC) simulations. Moreover, empirical determinations were made more accurate since more accurate spacecraft data have become available, combining them with information from NM latitude surveys [*Caballero-Lopez and Moraal*, 2012].

A detailed review of the present state of the art in yield function determination and a quantitative analysis of systematic effects are presented in *Maurin et al.* [2015]. Their Figure 8 of that article presents a comparison between the different yield functions that have been published recently or that are often used. The main observation is that the available functions are in fair agreement, but there are still major differences in the rigidity dependence and the absolute normalization. Comparisons between observed count rates and the most recent calculations still require relatively large station-dependent renormalization factors. For example, Table 1 of *Gil et al.* [2015] shows that a factor between 0.78 and 1.24 is necessary to renormalize the simulated count rate with respect to the observed count rate depending on the station, even if they obtain a good relative agreement when comparing with latitude survey data. This is related to the local environment and exact electronic setup of each station, which is not taken into account in general simulations. The type of neutron counter tube is also relevant, e.g., compared with the Canadian BP-28 counter, the Soviet analog CNM-15 has an efficiency that is lower by 15–20% [*Abunin et al.*, 2011; *Gil et al.*, 2015]. Moreover, the choice of hadronic generation model induces uncertainties of the order of 10% [*Mishev and Velinov*, 2014]. Assessing a single parameterization of the yield function that can be used for all NMs of the worldwide network from calculation only is challenging. Some extra information can be obtained by using a calibration monitor [*Krüger et al.*, 2008; *Krüger and Moraal*, 2010] that can be moved from station to station in order to measure intercalibration coefficients between stations. Results of such a calibration of the Princess Sirindhorn Neutron Monitor (PSNM) located at Doi Inthanon (DI), Thailand's highest mountain (altitude 2560 m), were presented in *Aiemsa-ad et al.* [2015]. Effects of the building surrounding the detector were estimated at the level of a few percent, both with simulations and by measurements with the calibrator. The effect of the electronic dead time was also estimated in simulations, and this can have a systematic effect of up to 30% on the count rate. The relevance of the electronic dead time has been recognized, and it plays a role in multiplicity and time delay distribution analyses [*Bieber et al.*, 2004; *Kollár et al.*, 2011; *Balabin*, 2013; *Ruffolo et al.*, 2016]. However, to the knowledge of the authors, a detailed analysis of the dead time dependence of the yield function has not been performed yet.

In the present work, we aim to develop accurate NM yield functions based on Monte Carlo (MC) simulations with no adjustable parameters. As a case study, we have performed a detailed analysis of the tube per tube count rate of the PSNM based on about 7 years of observations and on MC simulations of both the interaction of primary cosmic ray particles in Earth's atmosphere and the interaction of the SPs in the standard 18NM64 detector (i.e., 18-tube monitor of "NM64" design) [*Hatton and Carmichael*, 1964] with BP-28 tubes of the PSNM station. In section 2, we describe the methods used to simulate the distributions of SPs at ground level at the location of DI and the response of the PSNM to nine types of SPs. In section 3, we discuss the effects of the geomagnetic field and the dead time and on the simulated yield functions. In section 4, we analyze the tube-to-tube variations in count rate within the 18NM64. We propose normalization coefficients between standard NM64 detectors with different tube configurations.

2. Monte Carlo Simulations

We performed Monte Carlo simulations using the software FLUKA 2011-2c [*Ferrari et al.*, 2005; *Bohlen et al.*, 2014] with the interaction model DPMJET-2.5 (card HEAVYNUC). The method is composed of three stages (Figure 1): (i) the air shower development induced by the primary cosmic rays is simulated, and SP fluxes are extracted at the altitude of the detector plus six meters, (ii) with an independent simulation, the detector sensitivity within its surroundings is determined for nine types of secondary particles, and (iii) both simulations' outputs are combined to estimate the detector response to primary cosmic rays, yield functions, and count rates. Note that the atmospheric and detector geometry and SP beam dependence on incidence angle are the same as those used by *Aiemsa-ad et al.* [2015]. Here the simulation techniques were performed with a newer version of FLUKA and better statistics. The methodology of the detector response simulations is very different, and the SP beam area is now 4 times larger.

2.1. Interactions Due To Cosmic Rays in the Earth's Atmosphere

Models of the atmosphere typically provide profiles of temperature and pressure (or density) of the air (usually for dry conditions) with respect to altitude above a given location. It has been shown by *Abreu et al.* [2012] and *Moreno and Sciutto* [2013] that the widely used U.S. standard atmosphere of 1976 [*NASA*, 1976], determined for a latitude of ~45°N, induces significant discrepancies at other latitudes. Moreover, the model does not take into account moist air or seasonal variation. In order to account for those effects, the atmospheric profile of the present work (and also *Aiemsa-ad et al.* [2015]) combines information from two models:

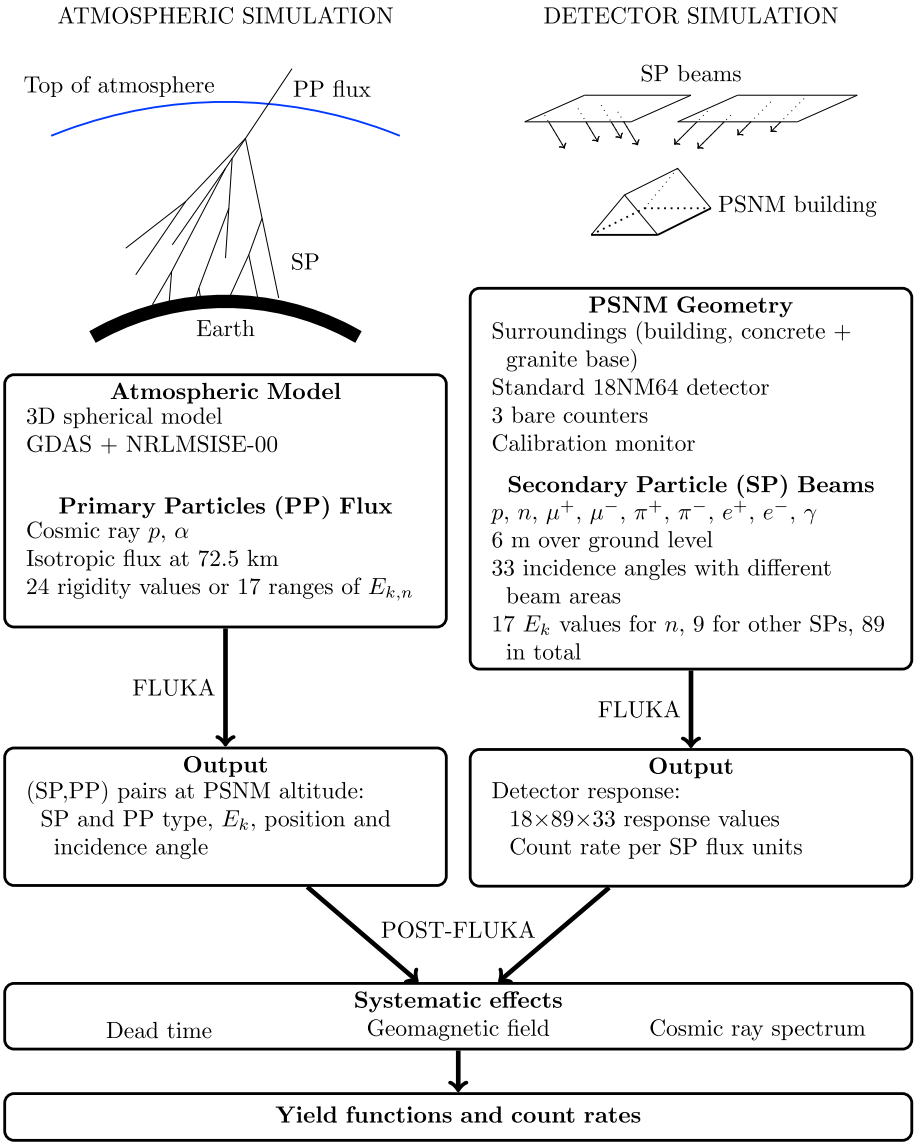

Figure 1. Methodology of Monte Carlo simulation for the Princess Sirindhorn Neutron Monitor (PSNM) at Doi Inthanon, Thailand, based on a combination of atmospheric simulation and detector simulation. See text for details.

the Global Data Assimilation System database (GDAS, http://ready.arl.noaa.gov/gdas1.php) at low altitude (which includes moist air), and the Naval Research Laboratory Mass Spectrometer, Incoherent Scatter Radar Extended model (NRLMSISE-00) [*Picone et al.*, 2002] for dry air at higher altitude. Details of our calculation of the profiles are presented in Appendix A. Most of our atmospheric simulations were performed using an atmospheric profile for Doi Inthanon in January (during the dry season from December to April), for a total pressure $P_{tot} = 751.1$ hPa and a partial water vapor pressure at the surface of $E_w = 6.3$ hPa, corresponding to an atmospheric depth of 769.9 g cm^{-2}.

The primary particles (PPs) we simulated were protons (up to 1000 GeV) and alphas (up to 2000 GeV). The injection point of the PP is located high in the Earth's atmosphere (altitude of 72 km) above the detector. The PP distributions were initially assumed to be isotropic; afterward, the effect of the geomagnetic field may be imposed (see below). The transport of PPs and their interaction products (secondary particles, SPs) through the atmosphere is determined without using a geomagnetic field. The simulations are performed for different ranges of PP (kinetic) energies, and the PP energy distribution is assumed to be uniform within that range. In postsimulation we apply energy-dependent weights according to the chosen cosmic ray spectrum at the top of the atmosphere.

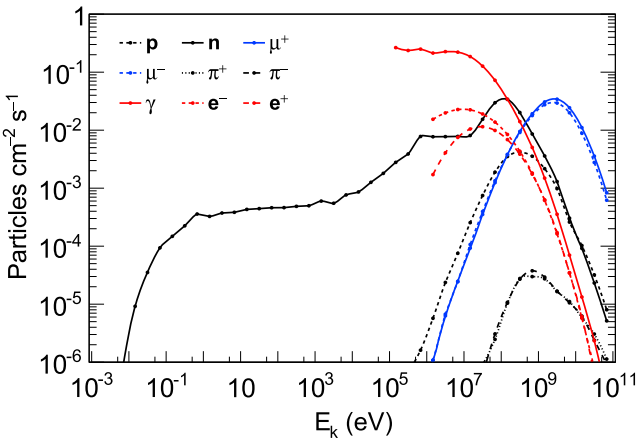

Figure 2. Simulated fluxes of various types of secondary particles at 6 m above the floor of the PSNM building from each bin in kinetic energy. Markers are plotted at the centers of bins of equal width in logarithmic scale.

The simulation of the atmospheric cascade development stops at a boundary 6 m above ground level at the altitude of the detector. The boundary is taken to be a sphere around the Earth. At the boundary, protons, neutrons, μ^+, μ^-, π^+, π^-, e^+, e^-, and γ are recorded with their characteristics and those of their parent PP. Depending on the incidence angle and the energy of the PP, the position of the SPs can spread over a large area around the latitude and longitude of the injection point. The difference of location can be larger than ~1° in both directions. Assuming spherical symmetry, each SP is translated over the boundary sphere to the detector location, and its parent PP is translated along with it. This procedure includes all SPs, taking into account the lateral extension of the atmospheric shower as well as the difference of spectrum between the core of the shower and the edge. Thus, we do not need to apply the geometric factor presented in *Mishev et al.* [2013].

In some cases we include the effect of the geomagnetic field by back tracing the antiparticle of the PP along the reversed trajectory through a model geomagnetic field. The (SP,PP) pair is rejected if the reversed anti-PP trajectory is not allowed, i.e., if it intercepts the Earth and does not connect with outer space. The International Geomagnetic Reference Field (IGRF-11) is used in this work with the techniques of *Lin et al.* [1995].

The simulated SP fluxes as a function of kinetic energy are presented in Figure 2. The SP fluxes at the ground level are determined using a PP distribution according to a Galactic cosmic ray spectrum at the top of the atmosphere, as described in section 2.3. Note that during the simulation, the production of electromagnetic components was cut below 1 MeV for $e^{\pm}$ and below 100 keV for γ. Those cuts are clearly visible in Figure 2. Here γ is the most abundant particle arriving at PSNM altitude, followed by n, μ^+, and μ^-. Then e^+, e^-, and p have lower fluxes, and π^- and π^+ fluxes are about 3 orders of magnitude lower.

2.2. Neutron Monitor Response to Secondary Particles

The response of the PSNM to the SPs has been estimated with a separate simulation, which explicitly includes particle scattering in all surrounding materials. The geometry of the 18NM64 and its surroundings has been included inside the FLUKA geometry editor as in *Aiemsa-ad et al.* [2015]; see their Figure 2. The PSNM building basically encompasses a 10 m × 10 m square and is covered by two roof panels slanted 45° from vertical, extending from near ground level on both sides to the peaked roof in the middle. The 18NM64 detector, with 18 neutron counter tubes in a single row, is placed on the concrete floor of the building [see also *Ruffolo et al.*, 2016, Figure 1]. Each BP-28 proportional counter tube is filled with BF_3 gas enriched to 95% ^{10}B, and neutrons are detected by the induced nuclear fission reaction $n+^{10}B \rightarrow {}^4He+{}^7Li$ and the characteristic signal due to ionization of the gas by the reaction products.

As shown by *Clem and Dorman* [2000], the contribution of nonvertical SPs is not negligible and must be taken into account in the Monte Carlo simulation. Because of this, numerous simulations have been performed for the nine types of SPs considered at varying kinetic energy E_k (for 17 values from 1 meV to 100 GeV for neutrons and for nine values from 1 MeV to 100 GeV for the eight other SP species) and varying incidence direction at five zenith angles θ (0°, 15°, 30°, 50°, and 70°) and eight azimuth angles φ (from 0° to 315°). Therefore, the total number of simulations of NM response is $(17+8\times9)\times(1+4\times8) = 89\times33 = 2937$. For vertical incidence, the beam is centered over the building and started at 6 m above the floor with a rectangular area of 34×30 m^2. For nonvertical incidence, the beam area is expanded depending on the incidence angle so that the beam covers the detector well, as described in *Aiemsa-ad et al.* [2015]. We define a count in the detector as a ^{10}B

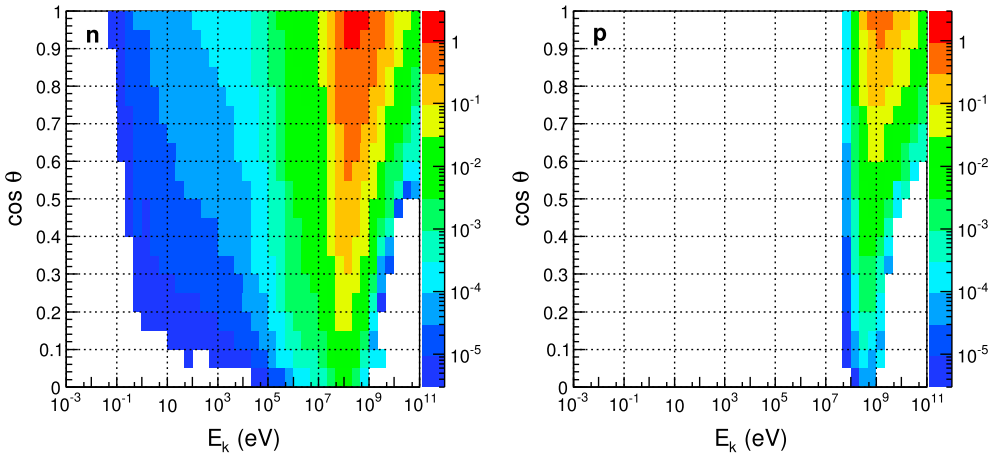

Figure 3. Simulated average count rate per tube at the PSNM due to secondary *n* (left) and *p* (right) as a function of the cosine of the zenith angle θ and of the kinetic energy E_k of the secondary particle. The palette of colors represents the average count rate per tube per bin (in Hz).

disintegration (due to neutron capture) in one of the neutron counter tubes. For each simulation, we obtain the response to SPs of type i, $R(i, j, \theta, \phi, E_k)$, expressed as counts (SP cm^{-2})$^{-1}$, where j is the tube number from 1 to 18.

2.3. Simulated Count Rate

The simulated count rate is determined by considering all (SP,PP) pairs from the first (atmospheric) simulation. A desired spectrum of the GCR at the top of the atmosphere can be applied by energy-dependent weight factors. Here we use directly measured proton and alpha-particle spectra from the Payload for Matter-Antimatter Exploration and Light-nuclei Astrophysics (PAMELA) spacecraft. For the primary proton spectrum, we combined data measured from 6 December 2009 to 1 January 2010 [*Adriani et al.*, 2013] at low energy ($\sigma_{syst} \sim 13\%$) with data for the period 2006–2008 [*Adriani et al.*, 2011] for $E_k > 48.62$ GeV, assuming negligible solar modulation over the latter energy range ($\sigma_{syst} \sim 4-5\%$). Note that the latter spectrum is lowered by 3.2% according to a footnote on page 4 of *Adriani et al.* [2013]. The primary He (alpha) spectrum corresponds only to the measurements for 2006–2008 from *Adriani et al.* [2011] ($\sigma_{syst} \sim 4-5\%$). For both primary species, a linear interpolation of $\log(J)$ versus $\log(E_{k,n})$ is used to determine the expected flux J at a given kinetic energy per nucleon $E_{k,n}$. Note that due to the interpolation along the kinetic energy, the detector response to photons with an energy in the range of the narrow photonuclear resonance in the lead (~10–15 MeV) is underestimated. This induces a systematic effect of ~0.2% on the simulated count rate.

A nonnegligible fraction of the actual NM count rate is due to the interaction of heavier cosmic nuclei in the atmosphere. Here their contribution is simulated by multiplying the He flux by an appropriate factor F_{hn}. As was well described by *Caballero-Lopez and Moraal* [2012], F_{hn} depends on the units used to express the flux. In the case of spectra from PAMELA, the He flux is measured. The heavier nuclei are assumed to contribute about 35.4% of the nucleons from cosmic rays with $Z > 1$ [*Caballero-Lopez and Moraal*, 2012, Table 3]. The PAMELA He spectrum in terms of kinetic energy per nucleon is consequently multiplied by $F_{hn,T} = 1.548$ (the rigidity spectrum would be multiplied by $F_{hn,P} = 1.584$).

The appropriate weight is applied to each (SP,PP) pair, and the induced count rate is estimated from the response values $R(i, j, \theta, \phi, E_k)$ of the second simulation. First, the response R is linearly interpolated along ϕ. Then a bilinear interpolation of $\log(R)$ versus $\log(E_k)$ and θ determines the response of the detector for the pair (SP,PP). For SPs with an incident zenith angle greater than 70°, the extrapolation uses the variation of the response between 50° and 70°. Nearly 10^8 SPs are used to estimate the simulated count rate. We obtained a simulated hourly count rate of 2.423×10^6. The mean observed count rate during December 2009 was 2.237×10^6. The simulation overestimates the observation by about 8.3%. Considering the systematic uncertainties in the spectra at the top of the atmosphere and in the heavy nucleus contribution, we are satisfied with this level of agreement.

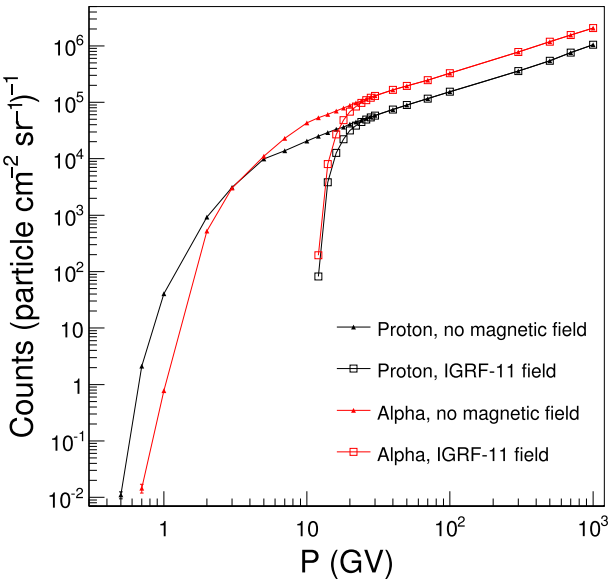

Figure 4. Calculated yield functions of the PSNM at Doi Inthanon, Thailand (altitude 2560 m), for the actual dead time. Before including the geomagnetic field, the results indicate an atmospheric cutoff at ~1 GV corresponding to the energy needed to create atmospheric secondary particles that can be detected at mountain altitude. When including the IGRF-11 model geomagnetic field, the yield function has a geomagnetic cutoff at ~17 GV.

From earlier simulations, *Aiemsa-ad et al.* [2015] showed results for the relative contributions of various SP species to the PSNM count rate. In the present simulations, about 96% of the count rate is induced by neutrons and protons. For both of these SPs, Figure 3 presents the average count rate per tube as function of the zenith angle cosine and kinetic energy of the SP. For reference, note that the total count rate per tube at PSNM is about 34 Hz. As expected, the energy range of the contributing neutrons is much broader than for the contributing protons, which also tend to produce counts at a higher energy than neutrons. We clearly see that the nonvertical incoming SPs contribute significantly to total count rate. About 21% of the total count rate is coming from neutrons with $\cos\theta < 0.7$.

3. Yield Functions

The yield functions (count rate per PP intensity) were calculated using simulations with monoenergetic and isotropic beams of protons and alphas at the top of the atmosphere from a rigidity of 500 MV to 1000 GV. Then a total of 325 million SPs were analyzed. Two sources of systematic effects were studied: (i) the geomagnetic field and (ii) the electronic dead time t_d. Depending on the electronics unit for each of the 18 neutron counter tubes in PSNM, the measured t_d values are between 19 and 29 μs. Other NMs in the worldwide network have used dead times ranging from 10 to 1200 μs [e.g., *Balabin et al.*, 2015].

Figure 4 and Table 1 present the yield functions with and without the geomagnetic field for the actual dead time configuration of the detector. These yield functions illustrate the two physical effects that cut off the NM response at low energy or rigidity, giving the NM a narrower spectral response than other ground-based cosmic rays detectors, that depends on its location, which is indeed the purpose of the worldwide NM network. These two cutoffs are the atmospheric cutoff at ~1 GV, i.e., the energy range needed to generate atmospheric showers detected at the altitude of PSNM in the case of no geomagnetic effects (as found near the geomagnetic poles) and the geomagnetic cutoff. For PSNM, the effective vertical geomagnetic cutoff P_c is about 16.8 GV, which is the highest of any fixed NM station in the world.

Primary particles of higher energy induce a higher count rate. Over the rigidity range of $P = 60$ to 1000 GV, the yield functions are proportional to $P^{0.8}$, and are about a factor 2.1 higher for alphas than for protons. Note that these values would change with a change in dead time. Under 40 GV, the geomagnetic field has an effect on the yield functions. Along with the east-west asymmetry in the magnetic deflection, the geomagnetic cutoff depends on the PP incidence angle, and the rigidity cutoff is not perfectly sharp. A decrease of the yield function by >1% can be observed at 30 GV, which is ~13 GV higher than P_c at Doi Inthanon. At low rigidity, well below P_c, the sensitivity of the detector is not negligible. At 14 GV, the yield function is still 13% of that in the case of no geomagnetic field. The geomagnetic cutoff rigidity is independent of the PP species, which is why NM data are usually interpreted in terms of particle rigidity.

In order to estimate the effect of the dead time, t_d, in the simulations, we have also applied various values of t_d uniformly to all tubes. We compared the simulated PSNM responses for five values: (i) the ideal case $t_d = 0$ s, (ii) $t_d = 2 \times 10^{-5}$ s (a typical value within the range actually used at PSNM and numerous other NMs), (iii) $t_d = 1 \times 10^{-4}$ s, (iv) $t_d = 1.2 \times 10^{-3}$ s (one of the values used at the Apatity NM) [*Balabin et al.*, 2015], and (v) $t_d = 4 \times 10^{-3}$ s to avoid counting multiple neutrons due to the same PP [*Ruffolo et al.*, 2016]. For this comparison, we do not apply a geomagnetic field in the simulation, in order to examine the effect of the dead

Table 1. Proton and Alpha Yield Functions of PSNM With Actual Dead Times, With or Without the IGRF-11 Model Geomagnetic Field

	Counts per Primary Flux (cm^2 sr)			
	Proton		Alpha	
P (GV)	No Field	IGRF-11	No Field	IGRF-11
0.5	1.10e−02	—	—	—
0.7	2.11e+00	—	1.45e−02	—
1	4.04e+01	—	7.76e−01	—
2	9.25e+02	—	5.23e+02	—
3	3.12e+03	—	3.04e+03	—
5	9.87e+03	—	1.11e+04	—
7	1.39e+04	—	2.30e+04	—
10	2.06e+04	—	4.34e+04	—
12	2.50e+04	8.21e+01	5.34e+04	1.95e+02
14	2.92e+04	3.85e+03	6.14e+04	8.05e+03
16	3.33e+04	1.28e+04	7.03e+04	2.72e+04
18	3.62e+04	2.21e+04	7.94e+04	4.85e+04
20	4.11e+04	3.16e+04	8.84e+04	6.81e+04
22	4.47e+04	3.88e+04	9.74e+04	8.44e+04
24	4.85e+04	4.50e+04	1.06e+05	9.79e+04
26	5.17e+04	4.96e+04	1.14e+05	1.10e+05
28	5.52e+04	5.40e+04	1.23e+05	1.20e+05
30	5.86e+04	5.79e+04	1.31e+05	1.29e+05
40	7.45e+04	7.44e+04	1.67e+05	1.67e+05
50	8.92e+04	8.92e+04	1.95e+05	1.95e+05
70	1.16e+05	1.16e+05	2.47e+05	2.47e+05
100	1.54e+05	1.54e+05	3.27e+05	3.27e+05
300	3.59e+05	3.59e+05	7.81e+05	7.81e+05
500	5.47e+05	5.47e+05	1.19e+06	1.19e+06
700	7.60e+05	7.60e+05	1.55e+06	1.55e+06
1000	1.04e+06	1.04e+06	2.06e+06	2.06e+06

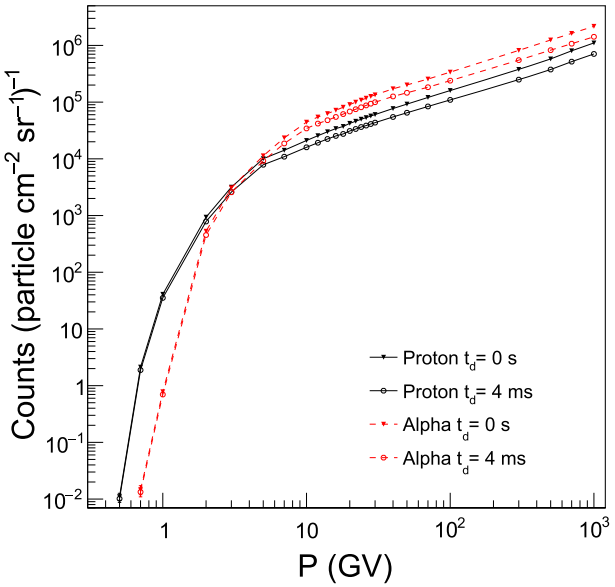

Figure 5. Calculated yield functions of the PSNM at Doi Inthanon, Thailand, for varying electronic dead time, t_d. In the simulation, the same dead time is applied to all 18 neutron counter tubes. A higher t_d leads to a lower yield function at high rigidity because of the increasing role of neutron multiplicity.

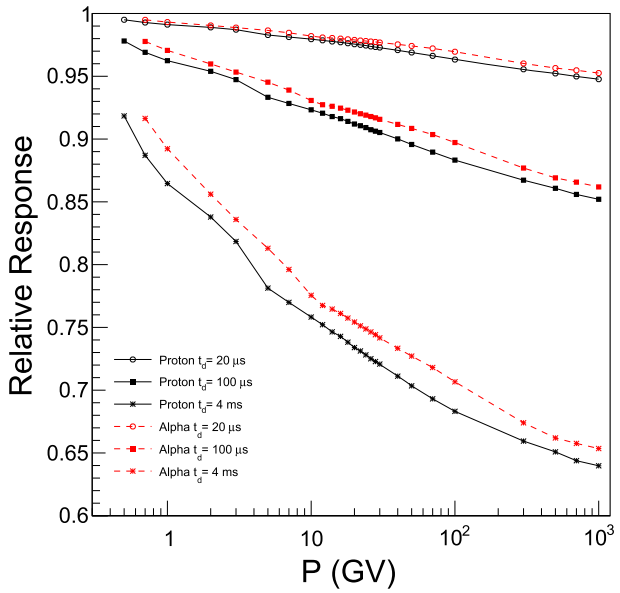

Figure 6. Relative yield functions with respect to the ideal case of no electronic dead time (t_d =0). There is a noticeable effect on the yield functions even for a typical value of t_d =20 µs.

Table 2. Proton Yield Functions of PSNM for Various Electronic Dead Times Without the Geomagnetic Field

	Counts per Primary Flux (cm^2 sr)				
P	Dead Time				
(GV)	0 s	20 µs	100 µs	1.2 ms	4 ms
0.5	1.11e−02	1.10e−02	1.08e−02	1.02e−02	1.02e−02
0.7	2.12e+00	2.11e+00	2.06e+00	1.90e+00	1.88e+00
1	4.08e+01	4.05e+01	3.93e+01	3.56e+01	3.53e+01
2	9.36e+02	9.26e+02	8.93e+02	7.93e+02	7.84e+02
3	3.17e+03	3.13e+03	3.00e+03	2.62e+03	2.59e+03
5	1.01e+04	9.89e+03	9.39e+03	7.99e+03	7.86e+03
7	1.42e+04	1.39e+04	1.31e+04	1.11e+04	1.09e+04
10	2.11e+04	2.06e+04	1.94e+04	1.63e+04	1.60e+04
12	2.56e+04	2.50e+04	2.35e+04	1.96e+04	1.92e+04
14	3.00e+04	2.93e+04	2.75e+04	2.28e+04	2.24e+04
16	3.41e+04	3.33e+04	3.13e+04	2.58e+04	2.54e+04
18	3.72e+04	3.63e+04	3.40e+04	2.80e+04	2.75e+04
20	4.22e+04	4.12e+04	3.85e+04	3.16e+04	3.10e+04
22	4.60e+04	4.48e+04	4.19e+04	3.43e+04	3.36e+04
24	5.00e+04	4.87e+04	4.54e+04	3.71e+04	3.64e+04
26	5.33e+04	5.19e+04	4.83e+04	3.94e+04	3.86e+04
28	5.69e+04	5.54e+04	5.15e+04	4.20e+04	4.11e+04
30	6.04e+04	5.87e+04	5.47e+04	4.45e+04	4.35e+04
40	7.69e+04	7.47e+04	6.93e+04	5.60e+04	5.47e+04
50	9.23e+04	8.95e+04	8.27e+04	6.65e+04	6.50e+04
70	1.21e+05	1.17e+05	1.08e+05	8.59e+04	8.39e+04
100	1.60e+05	1.54e+05	1.41e+05	1.12e+05	1.09e+05
300	3.78e+05	3.61e+05	3.28e+05	2.56e+05	2.49e+05
500	5.77e+05	5.50e+05	4.97e+05	3.87e+05	3.76e+05
700	8.04e+05	7.63e+05	6.88e+05	5.33e+05	5.17e+05
1000	1.11e+06	1.05e+06	9.42e+05	7.29e+05	7.07e+05

Table 3. Alpha Yield Functions of PSNM for Various Electronic Dead Times Without the Geomagnetic Field

	Counts per Primary Flux (cm^2 sr)				
P	Dead Time				
(GV)	0 s	20 μs	100 μs	1.2 ms	4 ms
0.5	—	—	—	—	—
0.7	1.46e−02	1.45e−02	1.43e−02	1.34e−02	1.34e−02
1	7.82e−01	7.77e−01	7.59e−01	7.02e−01	6.98e−01
2	5.29e+02	5.24e+02	5.08e+02	4.57e+02	4.53e+02
3	3.08e+03	3.04e+03	2.93e+03	2.60e+03	2.57e+03
5	1.13e+04	1.12e+04	1.07e+04	9.31e+03	9.19e+03
7	2.34e+04	2.31e+04	2.20e+04	1.89e+04	1.87e+04
10	4.43e+04	4.35e+04	4.12e+04	3.49e+04	3.44e+04
12	5.45e+04	5.35e+04	5.06e+04	4.26e+04	4.19e+04
14	6.27e+04	6.15e+04	5.81e+04	4.88e+04	4.80e+04
16	7.20e+04	7.05e+04	6.65e+04	5.57e+04	5.48e+04
18	8.13e+04	7.96e+04	7.50e+04	6.27e+04	6.15e+04
20	9.06e+04	8.87e+04	8.35e+04	6.96e+04	6.83e+04
22	9.98e+04	9.76e+04	9.18e+04	7.64e+04	7.49e+04
24	1.08e+05	1.06e+05	9.96e+04	8.27e+04	8.11e+04
26	1.17e+05	1.15e+05	1.08e+05	8.92e+04	8.75e+04
28	1.26e+05	1.23e+05	1.16e+05	9.56e+04	9.38e+04
30	1.34e+05	1.31e+05	1.23e+05	1.02e+05	9.96e+04
40	1.72e+05	1.68e+05	1.57e+05	1.29e+05	1.26e+05
50	2.01e+05	1.96e+05	1.83e+05	1.49e+05	1.46e+05
70	2.55e+05	2.48e+05	2.31e+05	1.87e+05	1.83e+05
100	3.38e+05	3.28e+05	3.03e+05	2.44e+05	2.39e+05
300	8.17e+05	7.84e+05	7.16e+05	5.65e+05	5.50e+05
500	1.25e+06	1.19e+06	1.08e+06	8.48e+05	8.25e+05
700	1.63e+06	1.56e+06	1.41e+06	1.10e+06	1.07e+06
1000	2.17e+06	2.07e+06	1.87e+06	1.46e+06	1.42e+06

time at all rigidities above the atmospheric cutoff. (Applying a model geomagnetic field would not change the effect of the dead time but would remove a wide range of rigidity from the analysis.) The results are presented in Figure 5. Applying a large dead time decreases the response functions, and the larger the rigidity of the primary particle, the larger the decrease is, because of the increasing role of neutron multiplicity, i.e., multiple neutron counts due to the same PP [*Hatton*, 1971]. This is more explicitly shown in Figure 6, which presents the relative yield functions with respect to the ideal case of zero dead time. At a given rigidity, the yield functions of the protons are more affected by the dead time than the alphas. This is due to the difference in kinetic energy per nucleon which is about 2 times lower for alphas than for protons. The yield function values for protons and alphas are presented in Tables 2 and 3, respectively. The NMs located at a high rigidity cutoff [see also *Aiemsa-ad et al.*, 2015] are more sensitive to the dead time value than NMs at high latitude or that are limited by the atmospheric cutoff.

A seasonal wave in the leader fraction (ratio of the number of SPs giving counts by the total number of counts) at PSNM, which is related to the time delay between counts and represents an inverse multiplicity, was observed by *Ruffolo et al.* [2016]. The results shown in the present work used an atmospheric profile for January (dry season). We also computed the yield functions using an atmospheric profile appropriate for the month of July (rainy season) to study the seasonal difference. Statistical uncertainties in the MC results were too large to study this effect, even after the yield functions were corrected for the change of atmospheric pressure using an empirical pressure correction (here assumed independent of rigidity). More work will be needed to estimate the seasonal effect.

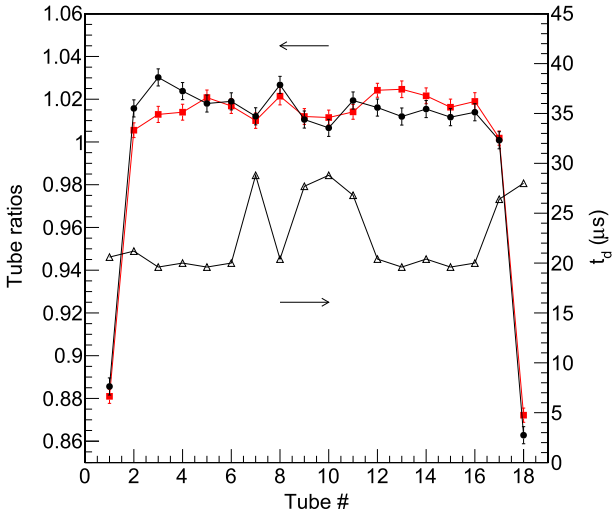

Figure 7. Count rate of each PSNM neutron counter tube relative to the tube average and measured electronic dead times. Observations are represented by filled circles. Simulated values are represented by filled squares. Dead time values are represented by open triangles. There are clear effects of the tube position relative to the edges of the row of 18 counter tubes and the dead time.

4. Dependence on the Configuration

The PSNM provides the count rates for each of its 18 proportional counters. This gives us the opportunity to study the tube dependence of the response, including the effects of tube position and dead time, from simulations and observations. We calculated the contribution of each tube to the total count rate. We define the 18 tube ratios as follows:

$$r_j = 18\frac{C_j}{C} \tag{1}$$

where C_j is the hourly count rate in tube j and C the hourly count rate summed over the 18 tubes. Figure 7 shows the distribution of the tube ratios at PSNM from July 2008 to November 2014. The data points represent the average of the hourly tube ratios and the error bars the standard deviations. The first observation that can be made is that the edge tubes 1 and 18 contribute over 10% less than the tubes in the center. This is explained by the fact that there is less lead producer near those tubes. The next-to-edge tubes are also affected but at a much lower level, ∼1%. Second, the tube ratios are anticorrelated with the values of the dead time and the effect is over 1% for a change in dead time from ∼20 to ∼27 µs. In December 2014, the tubes from positions 1 ($t_{d,1}$ = 20.6 µs) and 18 ($t_{d,18}$ = 28.0 µs) were switched. The contribution at position 1 decreased from 0.886 to 0.870, and that at position 18 increased from 0.863 to 0.881. This indicates a difference of 2% between the response functions of the different edge proportional counters, a difference that can mainly be attributed to the dead time difference (though additional effects such as counter efficiency cannot be excluded). Moreover, a small count rate asymmetry is observed between the two edge positions which is presumably due to asymmetry of the structure of the building and the surroundings, although their effect on the count asymmetry is weaker in the simulation.

As presented in Figure 7, we also calculated the tube ratios with the simulation described above. A very good agreement with the data is observed, and the effects of the dead time and position relative to the edge are well reproduced. There is a small linear trend in the observed count rate ratio versus tube position, which is not present in the simulation. This minor discrepancy could be due to approximations made in the geometry model of the building as well as simplification of the detection process: the efficiency of all proportional counters is assumed to be identical and differences in high voltage, electronic discriminators, and noise are not simulated.

The tube per tube analysis allows us to scale the response function of a standard NM64 detector depending on its configuration. In terms of the contribution of a center tube (not an edge or next-to-edge tube), taken to be 1, we define the normalization coefficient of an NM64 with N tubes as the count rate expressed as an equivalent number of center tubes. Because edge tubes have a lower count rate, the total normalization coefficient is less than N, not equal to N as assumed in some previous work. In the case of PSNM, the detector is composed of 14 center tubes with a normalized response per tube of T_C = 1 per tube, and two next-to-edge tubes and two edge tubes with observed relative responses of T_{E-1} = 0.992 and T_E = 0.860, respectively. Thus, PSNM is equivalent to an NM with 17.70 center tubes. The NM simulation for PSNM gives exactly the same normalization coefficient.

Table 4 lists the normalization coefficients for some common NM64 configurations, based on observations and MC simulations. The cases we consider that have groups of three tubes, 3NM64, and 6 × 3NM64 (i.e., 18 tubes arranged in six groups of three in a row), contain a special tube position that is next to both edges

Table 4. Normalization Coefficients Between Standard NM64 Configurations[a]

Configuration	T_C	T_{E-1}	T'_{E-1}	T_E	N_{Data}	N_{MC}	$N_{\text{MC,1.2 ms}}$
Data[b]	1	0.992	0.983	0.860			
MC[c]	1	0.987	0.974	0.862			
MC (t_d =1.2 ms)[d]	1	0.985	0.971	0.851			
3NM64	0	0	1	2	2.70	2.70	2.67
6NM64	2	2	0	2	5.70	5.70	5.67
12NM64	8	2	0	2	11.70	11.70	11.67
6 × 3NM64	0	0	6	12	16.22	16.18	16.04
3 × 6NM64	6	6	0	6	17.11	17.09	17.02
18NM64	14	2	0	2	17.70	17.70	17.67

[a] T_C, T_{E-1}, and T_E are the center, next-to-edge, and edge tubes, respectively. T'_{E-1} is for the next-to-edge tube in a set of three tubes, which is not directly measured or simulated; we use $T'_{E-1} = 2T_{E-1} - 1$. N values are normalization coefficients, i.e., expected count rate divided by count rate of a center tube.
[b] Measured from PSNM (18NM64, P_c =16.8 GV, altitude 2560 m).
[c] Monte Carlo simulation results for PSNM.
[d] Monte Carlo simulation results for PSNM, applying a dead time of 1.2 ms.

in its group. This type of tube is neither observed nor simulated for PSNM. Here we estimate the normalization coefficient for such a tube as $T'_{E-1} = 2T_{E-1} - 1$, i.e., doubling the deficit of T_{E-1} from 1 to account for proximity to two edges. Note here that the difference in count rate between a 6×3NM64 and an 18NM64 is about 9%.

The effect of the dead time was simulated by assuming a single value for all the tubes. Based on the time delay distributions [*Ruffolo et al.*, 2016], applying a 4 ms dead time removes the neutron multiplicity, which tends to be larger in the edge tubes (Figure 8). The simulated total normalization coefficient is then reduced by at most about 1% with respect to the case of a short dead time. Simulated normalization coefficients for the intermediate case of t_d = 1.2 ms, used at some NM stations, are shown in Table 4. The coefficients were also calculated for several atmospheric profiles at sea level, and these are consistent with the MC simulation results for the altitude and location of PSNM. Thus, these coefficients are quite insensitive to overlying matter or structure. The effect of the rigidity cutoff was also estimated, and the edge tube relative response increased only slightly from 0.862 to 0.867 when changing from a rigidity cutoff of 16.8 GV to no cutoff (no applied geomagnetic field). Finally, we obtained the same results within uncertainties to those for PSNM when using an atmospheric simulation for the NM at McMurdo, Antarctica, at sea level and at low P_c. These results indicate that these normalization coefficients estimated for PSNM should be accurate to within about 1% for any standard NM64 detector worldwide.

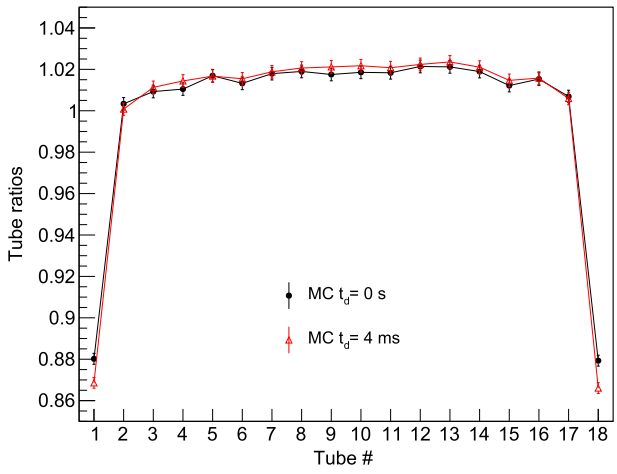

Figure 8. Simulated count rate of each PSNM neutron counter tube relative to the tube average for varying electronic dead time.

5. Summary

In order to improve the use of NM data, we developed an MC simulation of cosmic ray showers in the atmosphere and the NM detector response. We validated our techniques for the specific case of the PSNM at Doi Inthanon, Thailand (altitude 2560 m), the station with the world's highest cutoff rigidity (effective vertical cutoff at 16.8 GV), which expands the range of sensitivity of the worldwide NM network. We computed the yield functions of the PSNM detector for primary protons and alphas. The simulated count rate agrees

with the observations to within 9% for the recent solar minimum period, for which accurate GCR spectra are available from the PAMELA space mission. The geomagnetic field has a significant effect over a wide range of rigidity (12–40 GV) around its effective vertical rigidity cutoff. The dependence of the yield functions on the electronic dead time t_d was calculated, and effects as large as about 35% can be expected over the range of t_d values currently used by NMs. The sensitivity to variations of the GCR fluxes is also affected by this intrinsic characteristic of the NM. We encourage operators of NMs to provide information on the electronic dead times of their detectors (ideally tube-by-tube). The Neutron Monitor Database (http://www.nmdb.eu/) would be a good place to centralize the information. We also studied the dependence of neutron tube counter response on the counter position within the detector. Observations and the simulations agree reasonably well on the position and dead time dependence of the neutron counter rate, with a decrease larger than 10% for the edge tubes' response with respect to that of center tubes. Based on this, we determined normalization coefficients between standard NM64 detectors with different tube configurations. Effects on those coefficients due to the altitude, rigidity cutoff, and atmospheric profile at the location of the detector were estimated to be less than ~1% worldwide. Thus, we encourage the community to use these coefficients to significantly improve the comparison of count rates of NMs with different configurations.

Appendix A: The Atmospheric Model

The atmospheric profiles of the present work combine information from two models: the Global Data Assimilation System (GDAS) at low altitude (which includes moist air) and the Naval Research Laboratory Mass Spectrometer, Incoherent Scatter Radar Extended model (NRLMSISE-00) for dry air at higher altitude.

GDAS provides, every 6 h, a worldwide grid (with a granularity of 1° in latitude and longitude) of meteorological parameters computed from measured data (from weather stations, balloons, satellites, etc.). The parameters at a given location are determined by a bilinear interpolation from the four surrounding grid points' data. Data are available for 23 pressure surfaces from 1000 hPa to 20 hPa. The PSNM station is located at an altitude of 2560 m (~750 hPa), so only the layers with a pressure lower than 800 hPa are relevant for this analysis. The temperature T_{GDAS}, the pressure P_{GDAS} and the relative humidity RH are interpolated for each pressure surface.

Above the range of altitude of GDAS data (up to ≈26 km), the NRLMSISE-00 model provides the temperature and pressure profiles of the dry air at any altitude. In this analysis, the top of the atmosphere is set at an altitude of 72.5 km, which is around the limit of the homogeneous lower part of the atmosphere, and the values are taken for every 250 m. At the altitude boundary between the two models a linear interpolation is used.

A neutron monitor count rate significantly depends on the pressure and must be corrected. The pressure is thus constantly monitored during operation. In order to check the reliability of the GDAS data, we compared the altitude of the pressure layer 750 hPa with the altitude of the detector. During the month of January, the layer has on average an altitude of 2576 m that is slightly higher that the altitude of PSNM. This indicates that the pressure at PSNM altitude is slightly higher than 750 hPa. This is consistent with the average pressure measured by the Digiquartz barometer (from Paroscientific, Inc.) at Doi Inthanon that reports an average pressure of 751.1 hPa for the same period. Regarding the interpolation and the experimental conditions, these results show a reliable agreement between the model and the data.

The simulated atmosphere is divided into concentric spherical layers of 250 m height. The lowest part, from ground level (detector altitude), is separated into five layers with boundaries at 6 m, 10 m, 20 m, and 50 m above ground. The radius of Earth depends on the geodetic latitude of the neutron monitor. The atmospheric layers are defined as a mixture of dry air and water vapor with a constant composition, temperature, and pressure within a layer. The air is assumed to be an ideal gas. The volume fractions of the dry air in the homogeneous atmosphere are $F_{N_2} = 0.781$, $F_{O_2} = 0.210$, and $F_{Ar} = 0.009$ as derived from *Pidwirny* [2006]. Its molar mass, M_{dry}, is defined as

$$M_{\mathrm{dry}} = F_{N_2} M_{N_2} + F_{O_2} M_{O_2} + F_{Ar} M_{Ar} \tag{A1}$$

where $M_{N_2} = 28.0134$ g mol^{-1}, $M_{O_2} = 31.9988$ g mol^{-1}, and $M_{Ar} = 39.948$ g mol^{-1}. The molar mass of water vapor, M_{wv}, is defined as

$$M_{\mathrm{wv}} = 2M_H + M_O \tag{A2}$$

where $M_H = 1.0079$ g mol^{-1} and $M_O = 15.9994$ g mol^{-1}.

The knowledge of the density profile is crucial to accurately simulating the development of the showers produced by the primary cosmic rays. The density ρ_{air} (in kg m^{-3}) is calculated using the ideal gas law:

$$\rho_{\text{air}} = \frac{P_{\text{air}} M_{air}}{R T_{\text{air}}} \tag{A3}$$

where P_{air} is the pressure of air (in Pa), M_{air} its molar mass (in kg mol^{-1}), T_{air} its temperature (in K) and $R = 8.31432$ J mol^{-1} K^{-1} the universal gas constant. At constant pressure (as assumed inside a layer), the water vapor is lighter than the dry air ($M_{\text{wv}} < M_{\text{dry}}$), so M_{air} is significantly dependent on the humidity and on the temperature of the layer. The higher the temperature is the more water vapor is present in the air and the lower is M_{air}. The maximum amount of water that air can handle can be quantified by the saturated water vapor pressure E_{ws} (in hPa), which is determined by the following formula (from *World Meteorological Organization* [2008]):

$$E_{\text{ws}} = 6.112 \times \exp\left(\frac{17.62T}{T + 243.12}\right) \tag{A4}$$

where T is expressed in degrees Celsius. The water vapor pressure E_{wv} can then be deduced from the relative humidity RH (in %) via

$$E_{\text{wv}} = E_{\text{ws}} \times \frac{\text{RH}}{100}. \tag{A5}$$

The moist air is also assumed to be an ideal gas so the pressure of dry air is $P_{\text{dry}} = P_{\text{air}} - E_{\text{wv}}$, where $P_{\text{air}} = P_{\text{GDAS}}$ in our case. The air density of each layer is then defined as

$$\rho_{\text{air}} = \rho_{\text{dry}} + \rho_{\text{wv}} = \frac{P_{\text{dry}} M_{\text{dry}}}{R T_{\text{GDAS}}} + \frac{E_{\text{wv}} M_{\text{wv}}}{R T_{\text{GDAS}}}. \tag{A6}$$

Once the density of the air is calculated for a layer, the pressure of the next upper layer is defined using the hydrostatic equilibrium assumption, i.e., the pressure induced by a column of air corresponds to the weight of the column. As the total pressure is known from in situ monitoring, the pressure of each layer is computed recursively by subtracting the pressure induced by the column of air of the lower layers from the ground pressure P_G which is the mean value of the pressure measured at the location of the detector during the period of interest. The pressure of the $(k+1)$th layer is calculated by

$$P_{k+1} = P_k - g_k \rho_k H_k, k > 1 \tag{A7}$$

$$P_1 = P_G, \tag{A8}$$

where g_k (in m s^{-2}), ρ_k (in kg m^{-3}), and H_k (in m) are, respectively, the acceleration of gravity at the altitude of the lower boundary of the k^{th} layer, the density, and the height of the kth layer. The decrease of g_k with altitude is taken into account as follows. The model of gravity used is WGS84 [*National Imagery and Mapping Agency*, 1997]. It defines the normal gravity on an ellipsoidal surface based on the formula of Somigliana as

$$g_s(\Phi) = g_e \frac{1 + k \sin^2 \Phi}{\sqrt{1 - e^2 \sin^2 \Phi}} \tag{A9}$$

where e is first ellipsoidal eccentricity, Φ the geodetic latitude, and $k = bg_p/(ag_e) - 1$ with g_e and g_p the theoretical gravities at the equator and at the poles, respectively. The parameters a and b represent the semimajor and semiminor axes of the ellipsoid, respectively. At the altitude h, the gravitational acceleration is defined as

$$g(h, \Phi) = g_s(\Phi)\left[1 - \frac{2}{a}(1 + f + m - 2f \sin^2 \Phi)h + \frac{3}{a^2}h^2\right] \tag{A10}$$

where f is the flattening of the ellipsoid and $m = \omega^2 a^2 b/(GM)$ with ω representing the angular velocity of Earth and GM specifying the Earth's gravitational field.

Acknowledgments
We thank the Royal Thai Air Force and Chatchai Injai for their kind assistance with the observations and Andrew Snodin for setting up and maintaining the computing cluster on which our simulations were performed. This work was partially supported under the postdoctoral research sponsorship of Mahidol University, by the United States National Science Foundation via awards PLR-1341562 and PLR-1245939, by the Thailand Research Fund (Basic Research Grant BRG5880009), and by the Science Achievement Scholarship of Thailand. The data displayed in the figures are available upon request to the corresponding author.

References

Abreu, P., et al. (2012), Description of atmospheric conditions at the Pierre Auger observatory using the Global Data Assimilation System (GDAS), *Astroparticle Phys.*, *35*, 591, doi:10.1016/j.astropartphys.2011.12.002.

Abunin, A. A., E. V. Pletnikov, A. L. Shchepetov, and V. G. Yanke (2011), Efficiency of detection for neutron detectors with different geometries, *Bull. Russ. Acad. Sci.*, *75*, 866–868, doi:10.3103/S1062873811060037.

Adriani, O., et al. (2011), PAMELA measurements of cosmic-ray proton and helium spectra, *Science*, *332*, 69–72, doi:10.1126/science.1199172.

Adriani, O., et al. (2013), Time dependence of the proton flux measured by PAMELA during the 2006 July–2009 December solar minimum, *Astrophys. J.*, *765*, 91, doi:10.1088/0004-637X/765/2/91.

Aiemsa-ad, N., et al. (2015), Measurement and simulation of neutron monitor count rate dependence on surrounding structure, *J. Geophys. Res. Space Physics*, *120*, 5253–5265, doi:10.1002/2015JA021249.

Balabin, Yu. V. (2013), Anomalous barometric coefficient of microsecond intervals in neutron monitor, paper presented at 33rd International Cosmic Ray Conference, vol. 3, 1615, Sociedade Brasileira de Fisica, Rio de Janeiro, Brazil.

Balabin, Yu. V., E. Vashenyuk, B. Gvozdevsky, and A. Germanenko (2015), Upgrade of Apatity neutron monitor, *JPCS*, *632*, 12047, doi:10.1088/1742-6596/632/1/012047.

Bieber, J. W., J. M. Clem, M. L. Duldig, P. A. Evenson, J. E. Humble, and R. Pyle (2004), Latitude survey observations of neutron monitor multiplicity, *J. Geophys. Res.*, *109*, A12106, doi:10.1029/2004JA010493.

Bieber, J. W., J. Clem, P. Evenson, R. Pyle, A. Sáiz, and D. Ruffolo (2013), Giant ground level enhancement of relativistic solar protons on 2005 January 20. I. Spaceship Earth Observations, *Astrophys. J.*, *771*, 92, doi:10.1088/0004-637X/771/2/92.

Bohlen, T. T., F. Cerutti, M. P. W. Chin, A. Fassò, A. Ferrari, P. G. Ortega, A. Mairani, P. R. Sala, G. Smirnov, and V. Vlachoudis (2014), The FLUKA code: Developments and challenges for high energy and medical applications, *Nucl. Data Sheets*, *120*, 211–214.

Caballero-Lopez, R. A., and H. Moraal (2012), Cosmic-ray yield and response functions in the atmosphere, *J. Geophys. Res.*, *117*, A12103, doi:10.1029/2012JA011794.

Clem, J., and L. Dorman (2000), Neutron monitor response functions, *Space Sci. Rev.*, *93*, 335–359, doi:10.1023/A:1026508915269.

Ferrari, A., P. R. Sala, A. Fassò, and J. Ranft (2005), FLUKA: A multi-particle transport code, CERN-2005-10, INFN/TC_05/11, SLAC-R-773, CERN, Geneva.

Gil, A., I. G. Usoskin, G. A. Kovaltsov, A. L. Mishev, C. Corti, and V. Bindi (2015), Can we properly model the neutron monitor count rate?, *J. Geophys. Res. Space Physics*, *120*, 7172–7178, doi:10.1002/2015JA021654.

Hatton, C. J. (1971), *Progress in Elementary Particle and Cosmic Ray Physics, J. G. Wilson and S. A. Wouthuysen (Eds.)*, vol. 10, pp. 1–100, North-Holland, Amsterdam.

Hatton, C. J., and H. Carmichael (1964), Experimental investigation of the NM-64 neutron monitor, *Can. J. Phys.*, *42*, 2443–2472.

Kollár, V., K. Kudela, and M. Minarovjech (2011), Some alternative instrumentation for Galactic cosmic rays measurement using ground based neutron monitor detectors. I. Elapsed time methods, *Contrib. Astron. Obs. Skalnaté Pleso*, *41*, 5–14.

Krüger, H., and H. Moraal (2010), A calibration neutron monitor: Statistical accuracy and environmental sensitivity, *Adv. Space Res.*, *46*, 1394–1399, doi:10.1016/j.asr.201.07.008.

Krüger, H., H. Moraal, J. W. Bieber, J. M. Clem, P. A. Evenson, K. R. Pyle, M. L. Duldig, and J. E. Humble (2008), A calibration neutron monitor: Energy response and instrumental temperature sensitivity, *J. Geophys. Res.*, *113*, A08101, doi:10.1029/2008JA013229.

Lin, Z., J. W. Bieber, and P. Evenson (1995), Electron trajectories in a model magnetosphere: Simulation and observation under active conditions, *J. Geophys. Res.*, *100*, 23543–23550, doi:10.1029/95JA02696.

Maurin, D., A. Cheminet, L. Derome, A. Ghelfi, and G. Hubert (2015), Neutron monitors and muon detectors for solar modulation studies: Interstellar flux, yield function, and assessment of critical parameters in count rate calculations, *Adv. Space Res.*, *55*, 363–389, doi:10.1016/j.asr.2014.06.021.

Mishev, A. L., and P. I. Y. Velinov (2014), Influence of hadron and atmospheric models on computation of cosmic ray ionization in the atmosphere—Extension to heavy nuclei, *J. Atm. Sol. Terr. Phys.*, *120*, 111–120, doi:10.1016/j.jastp.2014.09.007.

Mishev, A. L., I. G. Usoskin, and G. A. Kovaltsov (2013), Neutron monitor yield function: New improved computations, *J. Geophys. Res. Space Physics*, *118*, 2783–2788, doi:10.1002/jgra.50325.

Moreno, J. C., and S. Sciutto (2013), Characterization of the atmospheric depth profile using the ground-level temperature: The case of Malargüe, Argentina, *Eur. Phys. J. Plus*, *128*, 104, doi:10.1140/epjp/i2013-13104-3.

National Aeronautics and Space Administration (NASA) (1976), U.S. Standard Atmosphere 1976, NASA-TM-X-74335, U.S. Govt. Print. Off., Washington, D. C.

National Imagery and Mapping Agency (1997), *Department of Defense World Geodetic System 1984, NIMA TR8350.2*, 3rd ed., NIMA, Bethesda, MD.

Picone, J. M., A. E. Hedin, D. P. Drob, and A. C. Aikin (2002), NRLMSISE-00 empirical model of the atmosphere: Statistical comparisons and scientific issues, *J. Geophys. Res.*, *107*(A12), 1468, doi:10.1029/2002JA009430.

Pidwirny, M. (2006), Chapter 7: Atmospheric composition, in *Fundamentals of Physical Geography*, 2nd ed. [Available at http://www.physicalgeography.net/fundamentals/7a.html.]

Ruffolo, D., et al. (2016), Monitoring short-term cosmic ray spectral variations using neutron monitor time delay measurements, *Astrophys. J.*, *817*, 38, doi:10.3847/0004-637X/817/1/38.

World Meteorological Organization (2008), *Guide to Meteorological Instruments and Methods of Observation*, 7th ed., WMO, Geneva.